Large Molecular and Dust Reservoir of a Gravitationally Lensed Submillimeter Galaxy behind the Lupus I Molecular Cloud

N.B. When citing this work, cite the original published paper.

(article starts on next page)

Large Molecular and Dust Reservoir of a Gravitationally Lensed Submillimeter Galaxy behind the Lupus I Molecular Cloud

Yoichi Tamura[1] , Akio Taniguchi[1,2] , Tom J. L. C. Bakx[3] , Itziar De Gregorio-Monsalvo[4] , Masato Hagimoto[1] ,
Soh Ikarashi[5,6,7], Ryohei Kawabe[7,8] , Kotaro Kohno[9,10] , Kouichiro Nakanishi[7,8] , Tatsuya Takekoshi[2] ,
Yoshito Shimajiri[11] , Takashi Tsukagoshi[12] , Bunyo Hatsukade[7,8] , Daisuke Iono[7,8] , Hideo Matsuhara[8,13],
Kazuya Saigo[14] , and Masao Saito[7]

[1] Department of Physics, Graduate School of Science, Nagoya University, Furo, Chikusa, Nagoya, Aichi 464-8602, Japan; ytamura@nagoya-u.jp
[2] Kitami Institute of Technology, 165 Koen-cho, Kitami, Hokkaido 090-8507, Japan
[3] Department of Space, Earth, & Environment, Chalmers University of Technology, Chalmersplatsen 4, Gothenburg SE-412 96, Sweden
[4] European Southern Observatory, Alonso de Cordova 3107, Casilla 19, Vitacura, Santiago, Chile
[5] Junior College, Fukuoka Institute of Technology, 3-30-1 Wajiro-higashi, Higashi-ku, Fukuoka 811-0925, Japan
[6] Department of Physics, General Studies, College of Engineering, Nihon University, 1 Nakagawara, Tokusada, Tamuramachi, Koriyama, Fukushima, 963-8642,
Japan
[7] National Astronomical Observatory of Japan, 2-21-1 Osawa, Mitaka, Tokyo 181-8588, Japan
[8] The Graduate University for Advanced Studies (SOKENDAI), Shonan Village, Hayama, Kanagawa 240-0193, Japan
[9] Institute of Astronomy, Graduate School of Science, The University of Tokyo, 2-21-1 Osawa, Mitaka, Tokyo 181-0015, Japan
[10] Research Center for the Early Universe, Graduate School of Science, The University of Tokyo, 7-3-1 Hongo, Bunkyo-ku, Tokyo 113-0033, Japan
[11] Kyushu Kyoritsu University, 1-8 Jiyugaoka, Yahatanishi-ku, Kitakyushu, Fukuoka 807-0858, Japan
[12] Faculty of Engineering, Ashikaga University, 268-1 Ohmae-cho, Ashikaga, Tochigi 326-8558, Japan
[13] Institute of Space and Astronautical Science, Japan Aerospace Exploration Agency, 3-1-1 Yoshinodai, Chuo-ku, Sagamihara, Kanagawa 252-5210, Japan
[14] Department of Physics and Astronomy, Graduate School of Science and Engineering, Kagoshima University, 1-21-35 Korimoto, Kagoshima 890-0065, Japan

Abstract

We report the Australian Telescope Compact Array and Nobeyama 45 m telescope detection of a remarkably bright ($S_{1.1mm} = 44$ mJy) submillimeter galaxy MM J154506.4−344318 in emission lines at 48.5 and 97.0 GHz, respectively. We also identify part of an emission line at ≈218.3 GHz using the Atacama Large Millimeter/ submillimeter Array (ALMA). Together with photometric redshift estimates and the ratio between the line and infrared luminosities, we conclude that the emission lines are most likely to be the $J = 2$–1, 4–3, and 9–8 transitions of ^{12}CO at redshift $z = 3.753 \pm 0.001$. ALMA 1.3 mm continuum imaging reveals an arc and a spot separated by an angular distance of 1″6, indicative of a strongly lensed dusty star-forming galaxy with respective molecular and dust masses of $\log M_{mol}/M_\odot \approx 11.5$ and $\log M_{dust}/M_\odot \approx 9.4$ after being corrected for ≈6.6× gravitational magnification. The inferred dust-to-gas mass ratio is found to be high (≈0.0083) among coeval dusty star-forming galaxies, implying the presence of a massive, chemically enriched reservoir of cool interstellar medium at $z \approx 4$, or 1.6 Gyr after the Big Bang.

Unified Astronomy Thesaurus concepts: Galaxy formation (595); High-redshift galaxies (734); Interstellar medium (847); Starburst galaxies (1570); Strong gravitational lensing (1643); Submillimeter astronomy (1647)

1. Introduction

Pioneering (sub)millimeter extragalactic surveys by bolometer cameras on single-dish telescopes routinely discovered submillimeter galaxies (SMGs; A. W. Blain et al. 2002; C. M. Casey et al. 2014), dusty star-forming galaxies with $L_{IR} \gtrsim 10^{12}\ L_\odot$, providing a laboratory to understand extreme star formation, which cannot be seen in the local Universe. Armed with next-generation (sub)millimeter cameras, square-degree-scale surveys using far-infrared (FIR) to millimeter single-dish telescopes (e.g., Herschel, S. Eales et al. 2010; ASTE, K. S. Scott et al. 2012; APEX, A. Weiß et al. 2009; JCMT, J. E. Geach et al. 2017; T. K. Garratt et al. 2023; SPT, J. D. Vieira et al. 2010) yielded a number of extremely bright ($S_{1.1mm} \gtrsim 30$ mJy) SMGs, via early discovery and investigation of this extremely bright population of SMGs (e.g.,

A. M. Swinbank et al. 2010; S. Ikarashi et al. 2011; A. Omont et al. 2011).

Thanks to their apparent high luminosity by the aid of gravitational magnification, the *brightest* SMGs offer a unique opportunity to investigate their nature at the most intense peak (typical star formation rates (SFRs) of $\sim 10^3\ M_\odot\ \mathrm{yr}^{-1}$) of star formation (e.g., J. D. Vieira et al. 2013; J. S. Spilker et al. 2014, 2015; Z.-Y. Zhang et al. 2018; K. C. Litke et al. 2019; M. Rybak et al. 2020; G. Gururajan et al. 2022). However, the brightest SMGs are even brighter and rarer than existing (sub) millimeter-bright sources, such as Herschel-ATLAS/SDP (M. Negrello et al. 2010). It is indeed hard to spectroscopically identify such brightest SMGs owing to their optical faintness; only a couple of brightest SMGs are expected within ~10 deg^2 (e.g., T. Takekoshi et al. 2013).

MM J154506.4−344318 (hereafter MM J1545) was initially identified through the 4 deg^2 Lupus I molecular cloud survey carried out using the AzTEC 1.1 mm camera (G. W. Wilson et al. 2008) attached to the ASTE 10 m telescope (H. Ezawa et al. 2004, 2008), as an $S_{1.1mm} = 44 \pm 5$ mJy point-like object at the edge of the Lupus I molecular cloud. Indeed, the close proximity of this object to the molecular cloud misled us into

classifying it as an extremely dense starless core shortly ($\sim10^2$–10^3 yr) before protostar formation, which is only proposed theoretically (R. B. Larson 1969; K. Tomida et al. 2010).

Subsequent follow-up observations that we made using the Submillimeter Array (SMA), Very Large Array, ASTE, Nobeyama 45 m, Nobeyama Millimeter Array, Subaru/MOIRCS, and UKIRT/WFCAM, along with archival Spitzer (MIPS and IRAC) and Herschel (SPIRE) data, however, suggest a gravitationally lensed distant SMG at $z \sim 4$–5 (Y. Tamura et al. 2015). In particular, 6 cm and near-infrared (NIR) emission cannot be explained by any of the latest models of a starless core (e.g., K. Tomida et al. 2010, 2013). But a lensed SMG located far beyond the Lupus I cloud by chance (Y. Tamura et al. 2015) accounts for the multiwavelength properties and brightness at (sub)millimeter wavelengths if a low-z foreground galaxy seen in the NIR K_S band (J1545B) gravitationally magnifies it.

If this is the case, MM J1545 is the brightest of ~1400 SMGs found in the AzTEC/ASTE 1.1 mm deep extragalactic survey (e.g., K. Kohno et al. 2008; K. S. Scott et al. 2012) and places an interesting constraint on the physical properties of SMGs at the brightest end of 1.1 mm extragalactic source counts. The shallow slope of the counts at $S_{1.1mm} \sim 40$ mJy is also in favor of the presence of gravitational magnification (T. Takekoshi et al. 2013; Y. Tamura et al. 2015).[15]

In this paper, we report the detection of MM J1545 in several emission lines, which are most likely to be rotational transition lines of carbon monoxide (CO), using the Australian Telescope Compact Array (ATCA), the Nobeyama 45 m telescope, and the Atacama Large Millimeter/submillimeter Array (ALMA). We also present results of $0\farcs4$ resolution 1.3 mm continuum imaging with ALMA, suggesting the existence of gravitational magnification.

The rest of the paper is organized as follows: In Section 2 we describe observations carried out using the ATCA and Nobeyama 45 m telescopes. Section 3 describes the results. In Section 4 we discuss the results and summarize the paper.

Throughout this paper we use a concordance cosmology with the matter and dark energy densities $\Omega_m = 0.3$ and $\Omega_\Lambda = 0.7$, respectively, and a Hubble parameter $H_0 = 70$ km s^{-1} Mpc^{-1}.

2. Observations

2.1. ATCA Observations and Data Reduction

The ATCA observations covering 37–50 GHz were made on 2013 October 10–12 and 2014 April 4–6 (program ID: C2910). The array configurations employed in 2013 and 2014 were H214 and H168, respectively, while we do not use the longest baselines including the CA06 antenna because of their poor atmospheric phase stability. The resulting baseline length is in the range of 82–247 m and 61–192 m for the H214 and H168 configurations, respectively. The receivers were tuned to mostly cover the Q band of ATCA, which required five tuning setups covering 33.4–37.1 GHz, 36.9–40.6 GHz, 40.4–44.0 GHz, 43.6–47.2 GHz, and 46.8–50.4 GHz. The lowest-frequency setup, however, was flagged because of poor weather conditions. The Compact Array Broadband Backend

correlator was configured with the 1 MHz resolution mode for all of the receiver setups. The instrumental delay was checked and fixed using the bright radio source 3C 279 before starting the observing tracks. 3C 279 was also used for bandpass calibration. We observed J1451−375 ($S_{7mm} \approx 1$ Jy, 10.7 deg away from the target) every 10 minutes for complex gain calibration. Mars was observed once a night for absolute flux calibration. The absolute flux accuracy is estimated to be <20%.

Calibration and imaging were processed using the MIRIAD software (R. J. Sault et al. 1995). The data with poor phase stability were flagged before imaging. The resulting integration time per tuning was $\sim$80–90 minutes on average. The calibrated uv data were imaged using a natural weighting, and then the dirty image was beam deconvolved down to a 1σ level using MIRIAD tasks `invert` and `clean`, respectively. This yields a synthesized beam size of $5\farcs8 \times 3\farcs7$ (PA = $+81°$) at 48.6 GHz. The resulting rms noise levels for a spectral cube with a 200 km s^{-1} resolution and a continuum image integrated over 13 GHz are 0.7–1.1 mJy beam^{-1} (depending on observed frequencies) and 0.036 mJy beam^{-1}, respectively.

2.2. Nobeyama 45 m Observations and Data Reduction

In order to observe an upper-state transition of the emission line detected with ATCA, we carried out the 45 m observations during two periods, 2015 February 25–March 4 (ID: CG 141007) and 2016 February 26–March 8 (program ID: CG 151009). Because of the low decl. of the source ($\delta \approx -35°$), the elevation angle at Nobeyama is in the range of $\sim$15°–20°. We used the two-beam dual-polarization TZ receiver (T. Nakajima et al. 2013) together with the SAM45 digital spectrometer equipped with four spectral windows, each of which has a 2048 MHz bandwidth and 4096 spectral channels (D. Iono et al. 2012). The receiver and spectrometer were tuned such that the lower sideband was centered at two slightly different frequencies, 96.8 and 97.0 GHz, in order to distinguish a broad spectral line in radio frequency from potential baseline wiggles of the intermediate-frequency (IF) bandpass. The beam size (half-power beamwidth) is 18″. The native velocity resolution of the spectrometer is $\approx$1.5 km s^{-1} per channel, whereas 64 adjacent channels were binned to achieve $\approx$100 km s^{-1} resolution. In total, four spectral windows were configured to cover four IFs of two beams and two polarizations.

During observations, we position-switched the two beams of TZ with a period of 20 s (visiting on and off positions for 5 s each, plus antenna slew time), so that one of the beams is always on source. Intensity calibration was made 2–3 times per hour by using the standard single-temperature chopper-wheel method. Note that the atmosphere is reasonably approximated by a plane-parallel slab even for such low elevation angles. The pointing was checked every 1 hr, and pointing accuracy during the runs was typically 3″ rms under moderate wind speeds <5 m s^{-1}. The focusing correction was made at the secondary mirror based on a model describing homologous deformation of the primary mirror, while no additional focusing correction was made, which potentially limited the accuracy of our aperture efficiency estimate. The standard calibration source M17SW was observed several times at similar elevation angles for aperture efficiency (η_{ap}) measurements. By comparing the observed peak temperature of CS (2–1) ($T_A^* = 3.6$ K) with a past measurement of its main-beam temperature ($T_{MB} = 9.0$ K),

---

[15] If a certain, small fraction of galaxies at the brightest end of the number counts are gravitationally magnified, the brightest end extends toward higher flux densities, making the slope of the counts shallower at the highest flux densities.

the main-beam efficiency was estimated to be $\eta_{MB} \approx 0.40$. If assuming a typical conversion of $\eta_{MB} = 1.2\eta_{ap}$,[16] $\eta_{ap} \approx 0.33$, which corresponds to a gain of ≈ 4.7 Jy K^{-1}. According to the 45 m status report in the 2015–2016 season,[17] this is 80% of the TZ aperture efficiency measured at 98 GHz at an elevation angle of $\approx 40°$, which is consistent with but slightly lower than the past estimates, which is likely due to the low elevation angles of our observations.

Prior to the data reduction, we selected the data with good pointing accuracy under good wind speeds (<3 m s^{-1}) and fair system noise temperatures ($T_{sys} < 200$ K), leaving the data taken on 2016 February 26–28 and March 1, 3, and 4. Flagging, spectral baselining, and coadding of the calibrated spectra were done using the ATNF Spectral Analysis Package (ASAP) shipped with CASA (version 5.0.0; CASA Team et al. 2022). We loaded the observed data (in the format of NEWSTARM. Ikeda et al. 2001) into CASA as the ASAP Scantable format. We then flagged the data with rms noise levels being higher than those expected from the nominal system noise temperature, where spectral baseline fluctuations likely dominate the noise levels of the instantaneous spectra. The resulting on-source time is 5.46 hr. The offset and slope of each 5 s spectrum are subtracted by fitting a linear function to the spectral baseline. The central ≈ 1000 km s^{-1} where the line is expected and the ≈ 200 km s^{-1} band edges were masked when the linear fitting is performed. The baseline-subtracted spectra are coadded with weighting of T_{sys}^{-2} to obtain the final spectrum. The resulting rms noise level with a 100 km s^{-1} resolution is 1.8 mJy.

2.3. ALMA Imaging

We used high angular resolution ALMA imaging data in order to search for another spectral line and to confirm the presence of strong lensing. As part of the Soul of Lupus with ALMA (SOLA; M. Saito et al. 2015) project, the 1 mm continuum data were taken on 2016 April 1 (ID: 2015.1.00512.S; PI: Itziar de Gregorio–Monsalvo) using the Band 6 receivers in the C36–2 to C36–3 configurations (A. Santamarìa-Miranda et al. 2021). The receivers were tuned at $\nu_{LO} = 225.267$ GHz (1.3 mm). The correlators with the frequency-division mode were configured so that one of the basebands covered 2×0.469 GHz for a local CO (2–1) line, whereas the rest were assigned to cover 3×1.875 GHz. The sky condition was reasonable with a precipitable water vapor of 1.6 mm. The complex gain was calibrated using a nearby radio-loud quasar J1534−3526. The bandpass calibration was performed on J1517−2422, which was also used as a secondary flux calibrator ($S_{233 GHz} = 2.17 \pm 0.11$ Jy on 2016 March 27). The resulting on-source time was 211 s.

The uv data were calibrated in a standard manner using CASA (ver. 4.5.3). The calibrated uv data were then imaged using the CASA task `clean` with natural weighting to make a spectral cube, resulting in a synthesized beam of $0\rlap{.}''95 \times 0\rlap{.}''82$ (PA $= -82°$) and rms noise level of 0.94 mJy beam^{-1} at a spectral resolution of 15.625 MHz. For continuum imaging, we employ the superuniform weighting to achieve a high spatial resolution, which yields a synthesized beam of $0\rlap{.}''51 \times 0\rlap{.}''46$

---

[16] Assuming a Gaussian approximation for the beam solid angle and an aperture illumination with −12 dB edge taper (J. W. M. Baars 2007).
[17] https://www.nro.nao.ac.jp/~nro45mrt/html/prop/eff/eff2015.html

(PA $= -69°$) and point-source sensitivity of 0.14 mJy beam^{-1}. The absolute flux accuracy is estimated to be 10%.

We also retrieved public pipeline-processed Band 3 and 7 images (ID: 2019.1.00245.S and 2018.1.00126.S; PI: Itziar de Gregorio-Monsalvo) from the ALMA data archive for a subsequent spectral energy distribution (SED) analysis (Section 4.2). The beam sizes of the Band 3 and 7 data are $2\rlap{.}''7 \times 2\rlap{.}''2$ and $0\rlap{.}''89 \times 0\rlap{.}''75$, respectively. The noise levels are 0.04 and 0.12 mJy beam^{-1}, respectively. The absolute flux accuracy is estimated to be 10%.

3. Results

3.1. CO Detections and Redshift Identification

Across the ATCA 37–50 GHz spectrum and the integrated intensity map in Figure 1, we detect an 8.6σ emission line at 48.5 GHz at a position of $(\alpha_{J2000}, \delta_{J2000}) = (15^h45^m6\rlap{.}^s35, -34° 43'17\rlap{.}''8)$, which is in agreement with the previous SMA position, $(\alpha_{J2000}, \delta_{J2000})=(15^h45^m6\rlap{.}^s347, = -34° 43'18\rlap{.}''18)$ (Y. Tamura et al. 2015). The offset between the ATCA and SMA positions is consistent with a statistical error $(0\rlap{.}''4 \pm 0\rlap{.}''3)$, strongly suggesting that the emission feature is the counterpart to MM J1545. The velocity width and continuum-subtracted flux of MM J1545 are 543 ± 106 km s^{-1} and $S\Delta V = 3.0 \pm 0.5$ Jy km s^{-1}, respectively, as listed in Table 1, which are typical among ^{12}CO emission lines found in lensed SMGs. As reported by Y. Tamura et al. (2015), we also detect the continuum emission at 0.21 ± 0.04 mJy. The 40.4 and 46.9 GHz flux densities are 0.18 ± 0.06 mJy and 0.23 ± 0.06 mJy, respectively, yielding the 7 mm spectral index of $\alpha \sim 1.4$, where α is defined as $S_\nu \propto \nu^\alpha$. As we will see in Section 4.2, we find that the obtained slope is shallower than what is expected for a single-component dust emission and that the flux density exceeds the prediction from the best-fitting modified blackbody, which suggests an additional contribution from an even lower T_{dust} component and/or free–free emission.

Figure 2 shows the resulting ATCA, 45 m, and ALMA spectra. The 45 m spectrum shows a broad 5.8σ emission line at 97.0 GHz and at a velocity resolution of 100 km s^{-1}, with a velocity-integrated flux of 6.5 ± 0.7 Jy km s^{-1}. The velocity width is 625 ± 120 km s^{-1}, which is in good agreement with that of ATCA (Table 1). The frequency is almost exactly twice that of the ATCA emission line, which supports that they are emission lines of two rotational transitions of CO, where the upper-state quantum numbers are related as $J_{45m} = 2J_{ATCA}$.

Furthermore, we found a 13σ enhancement at the edge (218.3 GHz) of one of the ALMA spectral windows. The enhancement is so bright that the most likely interpretation is the blue part of another CO transition. A slight spatial offset between the integrated intensity and 1.3 mm continuum images (see the inset of the ALMA spectrum in Figure 2) is probably caused by the blue part of the line being associated with the northern component of the western arc, which we will see in Section 3.2. If this is the case, the only solution that explains ATCA, 45 m, and ALMA detections is the CO (2–1), (4–3), and (9–8) transitions at the redshift of $z = 3.753 \pm 0.001$.

This is consistent with previous photometric redshift estimates derived from mid-IR-to-radio photometry and SED templates of dusty star-forming galaxies (Arp 220, SMM J2135−0201, and average SMG; L. Silva et al. 1998; M. Michałowski et al. 2010; A. M. Swinbank et al. 2010): $z = 4.67^{+0.88}_{-0.74}$, $4.06^{+0.92}_{-0.11}$, and $4.20^{+0.87}_{-0.64}$, respectively (Y. Tamura et al. 2015; all error bars
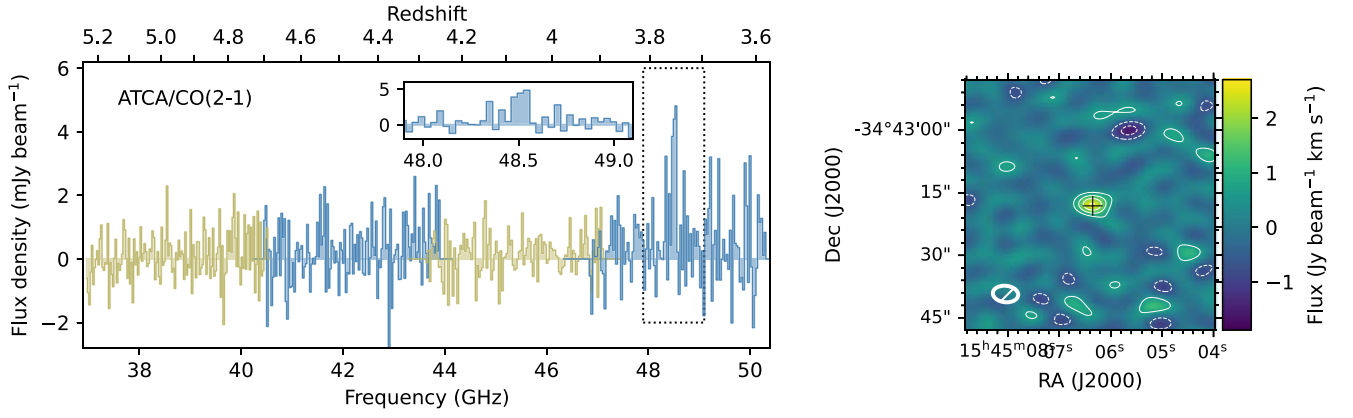
Figure 1. The ATCA spectrum and image of MM J1545. Left: the 13 GHz wide ATCA spectrum with a 200 km s^{-1} resolution. Four tunings are shown in different colors. The inset highlights the line feature outlined by the dotted box. The continuum is not subtracted. Right: the CO (2–1) integrated intensity image of MM J1545 taken with ATCA, which shows an 8.6σ line feature at the SMA position marked with a plus sign (Y. Tamura et al. 2015). The contours start at 2σ with a separation of 2σ. Negative values are shown with dashed contours. The synthesized beam size is indicated by an ellipse in the lower left corner.

Table 1
The ATCA and Nobeyama 45 m Results

Line	CO (2–1)	CO (4–3)
α_{J2000}	15$^{\mathrm{h}}$45$^{\mathrm{m}}$6$^{\mathrm{s}}$35	⋯
δ_{J2000}	−34°43′17″.8	⋯
Frequency (GHz)[a]	48.51 ± 0.007	96.99 ± 0.017
z_{CO}[a]	3.7523 ± 0.0006	3.7537 ± 0.0006
FWHM (km s^{-1})[a]	543 ± 106	625 ± 120
$S\Delta V$ (Jy km s^{-1})[b]	3.0 ± 0.5	6.5 ± 0.7
L'_{CO} (10^{11} K km s^{-1} pc^2)[c]	4.2 ± 0.7	2.3 ± 0.2
M_{mol} (10^{12} $M_\odot$)[c,d]	$1.9 \cdot \left(\frac{0.88}{R_{21}}\right)^{-1}$	$1.5 \cdot \left(\frac{0.52}{R_{41}}\right)^{-1}$

Notes.
[a] Value and error are derived from a single-component Gaussian fit.
[b] Value and error are derived from a spectral integration over a range of ±3$\bar{\sigma}$ from the observed-frame frequency of CO, i.e., $\nu_{\mathrm{CO}}/(1 + \bar{z})$, where $\bar{z}$ and $\bar{\sigma}$ are obtained from the average redshift ($z = 3.753$) and the average FWHM (590 km s^{-1}) between the two observations.
[c] Values are not corrected for lensing magnification.
[d] A CO (1–0)-to-M_{mol} conversion factor $\alpha_{\mathrm{CO}} = 4.0\ M_\odot$ (K km s^{-1} pc^2)$^{-1}$ (L. Dunne et al. 2022) is assumed. R_{21} and R_{41} are the CO (2–1)-to-CO (1–0) and CO (4–3)-to-CO (1–0) brightness temperature ratios, respectively. $R_{21} = 0.88 \pm 0.07$ and $R_{41} = 0.52 \pm 0.14$ (K. C. Harrington et al. 2021) are assumed throughout the paper.

represent the 68% confidence intervals). We find only a single line over the 13 GHz bandwidth of ATCA, which also places a redshift upper limit of $z < 7$ if the line is ^{12}CO. If the transitions are ($J = 1$–0 and 2–1) or ($J = 3$–2 and 6–5), the redshift would be $z = 1.876$ or 6.128, respectively, which are unlikely because they are well outside the photometric redshift estimates from the SED fits and cannot explain the ALMA spectrum.

In order to further assess the attribution of the lines, we use the L_{FIR}-to-L'_{CO} correlation (e.g., D. Iono et al. 2009) to predict a CO intensity at 48.5 GHz from the FIR luminosity of MM J1545 by following the prescription presented by Y. Tamura et al. (2014). If we assume the redshift of $z = 3.753$, the inferred FIR luminosity is estimated to be $\log L_{\mathrm{FIR}}/L_\odot \sim 13.5$–14 as presented in Section 4.2. This yields a CO (3–2) luminosity of $L'_{\mathrm{CO}} \sim 2 \times 10^{11}$ K km s^{-1} pc^2, which is almost similar to the CO (2–1) luminosity if assuming a typical
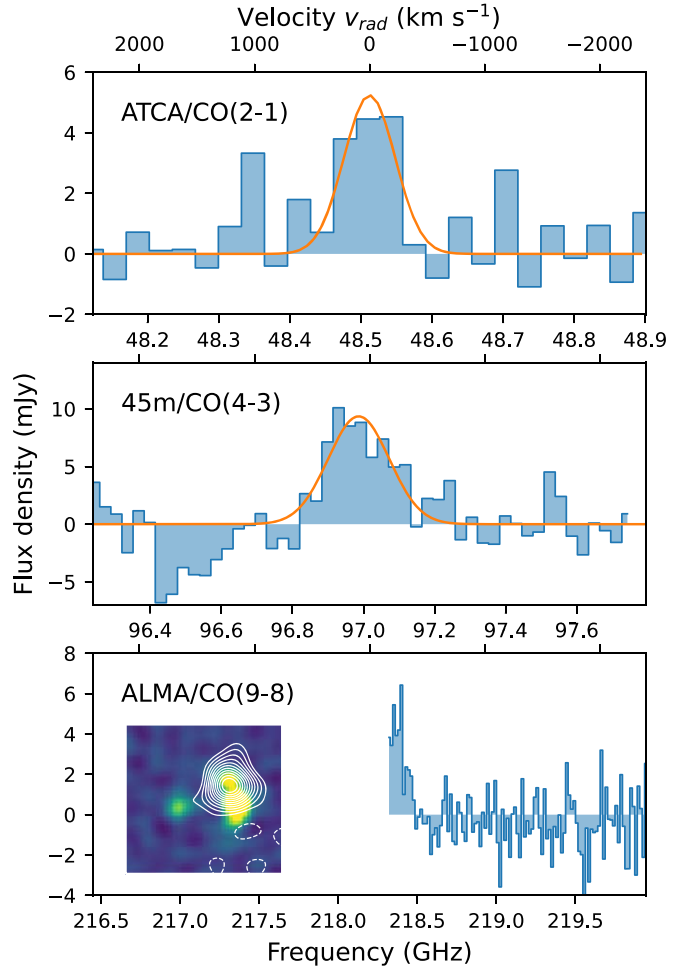

Figure 2. The CO spectrum of MM J1545. From top to bottom the ATCA, Nobeyama Radio Observatory 45 m, and ALMA Band 6 spectra are shown. The orange curve shows the best-fitting Gaussian. The inset in the bottom panel shows the 4″ × 4″ images of CO (9–8) (contours at −2σ, 2σ, 3σ, ⋯ , 13σ with σ = 63 mJy km s^{-1}) overlaid on the 1.3 mm continuum.

luminosity ratio of $L'_{\mathrm{CO(3-2)}}/L'_{\mathrm{CO(2-1)}} \gtrsim 0.88$ found in dusty star-forming galaxies (e.g., K. C. Harrington et al. 2021). The predicted flux is then $I_{\mathrm{CO\,(2-1)}} \sim 1$–2 Jy km s^{-1}, which is consistent with that observed at 48.5 GHz with ATCA. This also rules
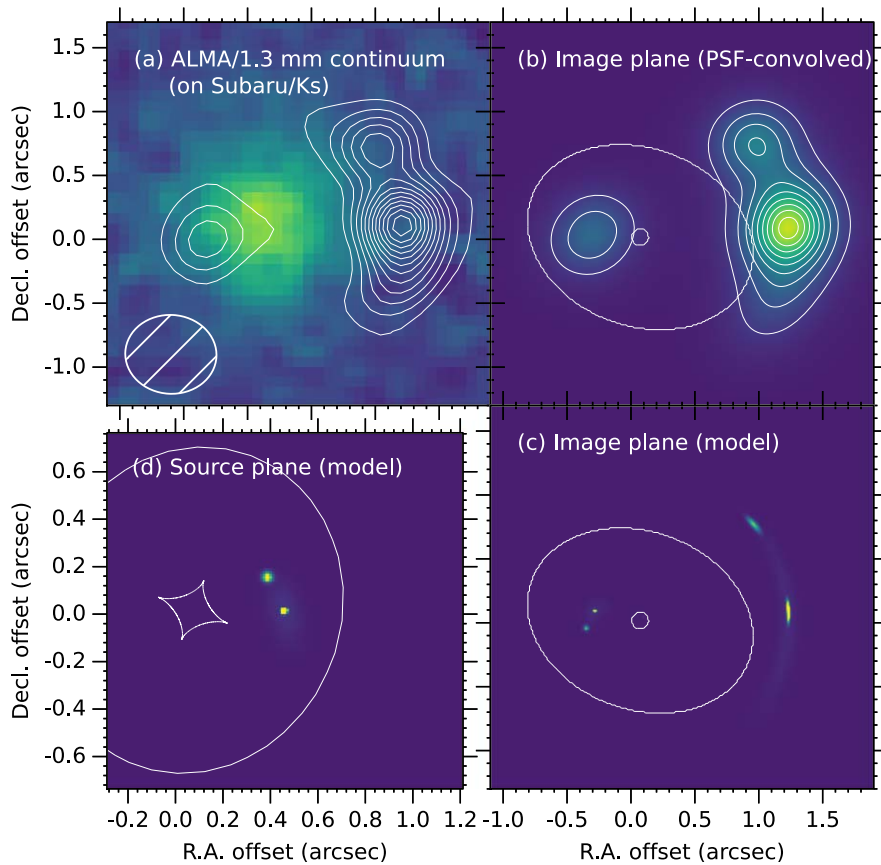
Figure 3. (a) The superuniform-weighted ALMA 1.3 mm continuum image (contours) overlaid on the Subaru/MOIRCS K_S-band image. The contours are drawn at $(5, 10, 15, \cdots) \times \sigma$, where $\sigma = 0.14$ mJy beam^{-1} is the 1σ noise level. The beam size is indicated by the hatched ellipse in the lower left corner. The K_S-band image shows the foreground lensing galaxy J1545B (Y. Tamura et al. 2015). (b) The modeled image plane brightness that is convolved by ALMA's point-spread function (PSF). The contours are drawn at 10%, 20%, $\cdots$ 90% of the peak brightness. The large and small ellipses represent the critical curve. (c) Same as panel (b), but deconvolved by the ALMA PSF. (d) The modeled source plane brightness with the caustics (solid curves).

out other possible lines, such as ^{13}CO, HCN, and HCO^{+}, since the non-^{12}CO lines should be an order of magnitude fainter. Thus, we conclude that the emission lines at 48.5, 97.0, and 218.2 GHz are attributed to three ^{12}CO rotational transitions of $J = 2-1$, $4-3$, and $9-8$, respectively.

3.2. ALMA Imaging and Gravitational Lens Model

As shown in Figure 3(a), the resulting ALMA continuum image reveals an arc to the west with an unresolved spot to the east, strongly suggesting the presence of strong lensing. The image shows at least two brightness peaks embedded in the western arc, suggesting two star-forming clumps embedded in this galaxy. We use the gravitational lens code, GLAFIC (M. Oguri 2010), to simply model the galaxy–galaxy lensing system. As a mass model, we assume a cored singular isothermal ellipsoid situated at $z = 0.5$. The photo-z of the lensing galaxy J1545B (Y. Tamura et al. 2015; see the background K_S-band image in Figure 3(a)) is not constrained very well, while the separation of $1''.6 \approx 2\theta_E$ is reproduced for $z = 0.5$ if the velocity dispersion of J1545B follows the NIR version of the Faber–Jackson relation (F. La Barbera et al. 2010), as discussed in Y. Tamura et al. (2015). We first use only the positions of the two peaks to roughly constrain the mass model. We then perform a χ^2 fit to the observed brightness distribution to put more stringent constraints on the mass model and intrinsic source brightness on the source plane.

Three two-dimensional Gaussians are used for realization of the source plane brightness: two compact axisymmetric Gaussians and an extended Gaussian to represent two brightness peaks and an extended diffuse component, respectively. Before applying the χ^2 fits, we smooth the modeled image plane with the clean beam of $0''.51 \times 0''.45$ (PA $= -69°$). We do not consider a model fit in the visibility domain for simplicity. We do not take an external shear into account because the degree of freedom is small. A noise level of $\sigma = 0.15$ mJy beam^{-1} is used for χ^2 calculation.

The results are shown in Figures 3(b), (c), and (d) for the image and source planes. The centroid of J1545B on the K_S-band image (Figure 3(a)) is in good agreement with the predicted position of the mass model. The velocity dispersion of the lens (200 km s^{-1}) is consistent with that estimated from the K_S-band version of the Faber–Jackson relation (F. La Barbera et al. 2010). The image plane reproduces the western arc with two clumps and the eastern spot, although the extended emission at low brightness levels is not reproduced very well. On the source plane, we find an interesting spatial structure that shows two bright spots embedded in an extended disk, while high-resolution imaging is necessary to confirm the detailed internal structure of MM J1545. The inferred magnification factor is $\mu_g = 6.6$, although this may have a large uncertainty depending on the extent of source plane brightness.

4. Discussions

4.1. Validity of the Magnification Factor

The ALMA image clearly reveals multiple images split by the strong gravitational lensing effect, while the angular resolution is still insufficient for full characterization of the lensing system, which limits the accuracy of the magnification factor. Instead, an excess of an observed CO luminosity from the correlation between (unlensed) CO (1–0) luminosity and velocity dispersion places an independent constraint on a magnification factor (A. I. Harris et al. 2012). This empirical luminosity–line width relation is similar to the Tully–Fisher relation (R. B. Tully & J. R. Fisher 1977) relating the luminosity and rotation velocity of spiral galaxies and has been characterized for CO emission of the SMG population (A. I. Harris et al. 2012; M. S. Bothwell et al. 2013) as

$$L_{CO}^{'11} = (\Delta V_{400})^{1.7}/3.5, \quad (1)$$

where $L_{CO}^{'11}$ are (unlensed) luminosities of CO (1–0) in units of $10^{11}\,\mathrm{K\,km\,s^{-1}\,pc^2}$ and ΔV_{400} is the FWHM line width in units of $400\,\mathrm{km\,s^{-1}}$. The $L_{CO}^{'}$–ΔV correlation of unlensed SMGs is known to be scattered because of unknown inclination angles of the SMGs, but this is still useful to roughly constrain the magnification factors of lensed SMGs.

As we will see in the next section, the molecular masses derived from CO (2–1) and (4–3) with their conversion factors, R_{21} and R_{41}, typically found among SMGs (e.g., K. C. Harrington et al. 2021; M. Hagimoto et al. 2023) are almost the same, suggesting that the inferred CO spectral line energy distribution of MM J1545 is similar to those found in SMGs. Thus, it is reasonable to assume $L_{CO}^{'11} = 3.7R_{21}^{-1} \approx 4.2$ derived from CO (2–1) for the CO (1–0) luminosity. Equation (1) predicts the CO (1–0) luminosity of $L_{CO}^{'11} = (543/400)^{1.7}/3.5 \approx 0.48$, which requires $\approx 9 \times$ magnification to reach the apparent CO (1–0) luminosity. Despite the ∼0.5 dex scatter in the L_{CO}–ΔV correlation, this is in reasonable agreement with the magnification factor we derived in Section 3.2. Hereafter we assume the magnification factor to be $\mu_g = 6.6$.

4.2. Intrinsic Properties

Figure 4 shows the rest-frame FIR-to-millimeter SED of MM J1545. In addition to photometry from the literature (Y. Tamura et al. 2015), archival ALMA Band 3 and 7 data are used. The aperture sizes we used for ALMA photometry are 3″5 (Band 3) and 2″0 (Bands 6 and 7). The modified blackbody fits yield the dust temperature $T_{dust} = 30.7^{+1.7}_{-1.5}\,\mathrm{K}$, the emissivity index $\beta_{dust} = 1.95^{+0.13}_{-0.12}$, and the apparent IR luminosity of $\log L_{IR}/L_\odot = 13.55 \pm 0.32$ if we take into account the heating from the cosmic microwave background ($T_{CMB} = 12.9\,\mathrm{K}$ at $z = 3.753$) following the expression by E. da Cunha et al. (2013). The emissivity index is higher than that previously obtained ($\beta_{dust} = 1.4$; Y. Tamura et al. 2015) because the new ALMA 3 mm photometry makes the Rayleigh–Jeans slope steeper. Although the origin of the flux excess at 7 mm is unknown, there could be an additional component such as a lower T_{dust} component, which can be confirmed by ALMA Band 1 observations.

If we take the magnification factor of $\mu_g = 6.6$, the delensed IR luminosity ($\log L_{IR}/L_\odot = 12.73 \pm 0.32$) and corresponding SFR (SFR $= 804^{+876}_{-419}\,M_\odot\,\mathrm{yr^{-1}}$ using the R. C. Kennicutt &
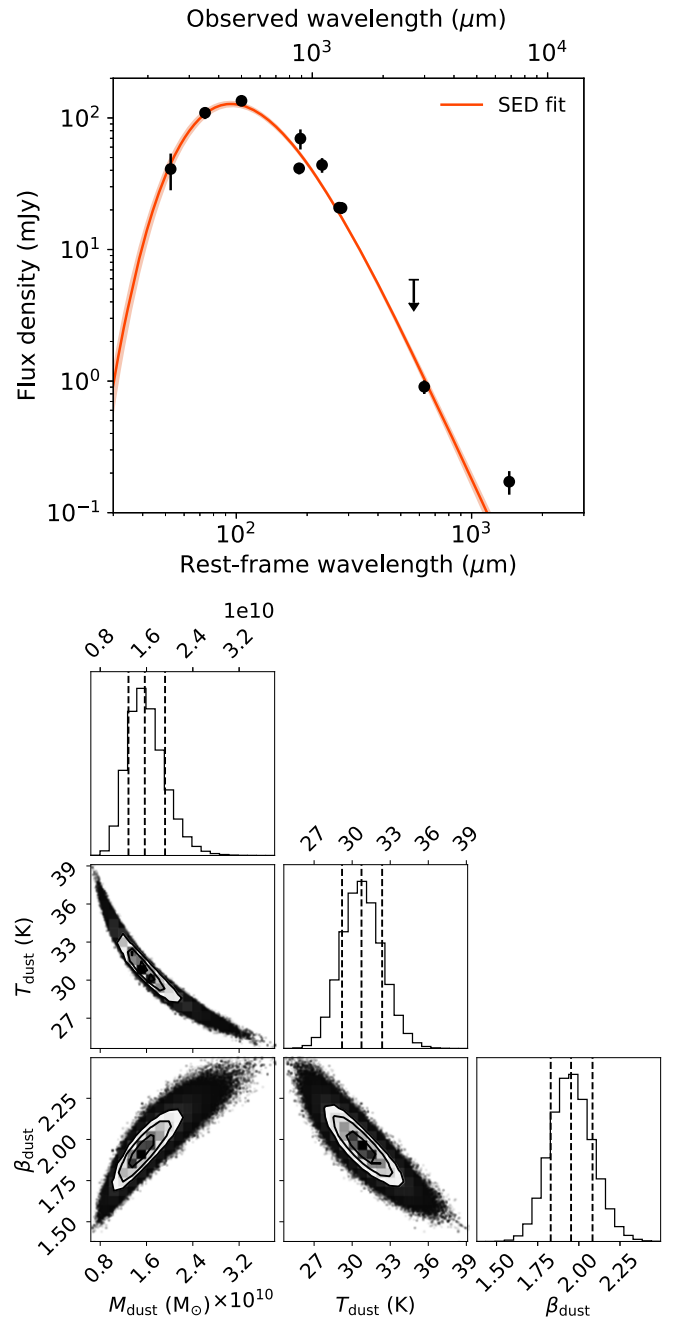

Figure 4. Top: the FIR-to-millimeter SED of MM J1545 (the red curve). The light-red band associated with the best-fitting SED represents the 68% confidence interval. Bottom: the posterior distribution function (pdf) of the parameters in the SED fits. The contours in the two-dimensional pdf are drawn at 1σ, 1.5σ, and 2σ. The vertical dashed lines in the marginalized one-dimensional pdf are shown at 16th, 50th, and 84th percentiles. The flux densities and the dust mass are not corrected for lensing magnification. See Section 4.2 for details.

N. J. Evans 2012 conversion with the P. Kroupa et al. 1993 initial mass function) are similar to those of unlensed SMGs, which are in the bright end ($S_{850\mu m} \approx 10\,\mathrm{mJy}$) of their number counts (e.g., J. E. Geach et al. 2017; B. Hatsukade et al. 2018; J. M. Simpson et al. 2020; S. Fujimoto et al. 2024).

Remarkably, the dust temperature found in MM J1545 is relatively low among the SMGs with a similar unlensed L_{IR} (e.g., C. Reuter et al. 2020), indicating a massive dust mass. If we approximate the dust mass absorption coefficient (κ_ν) as
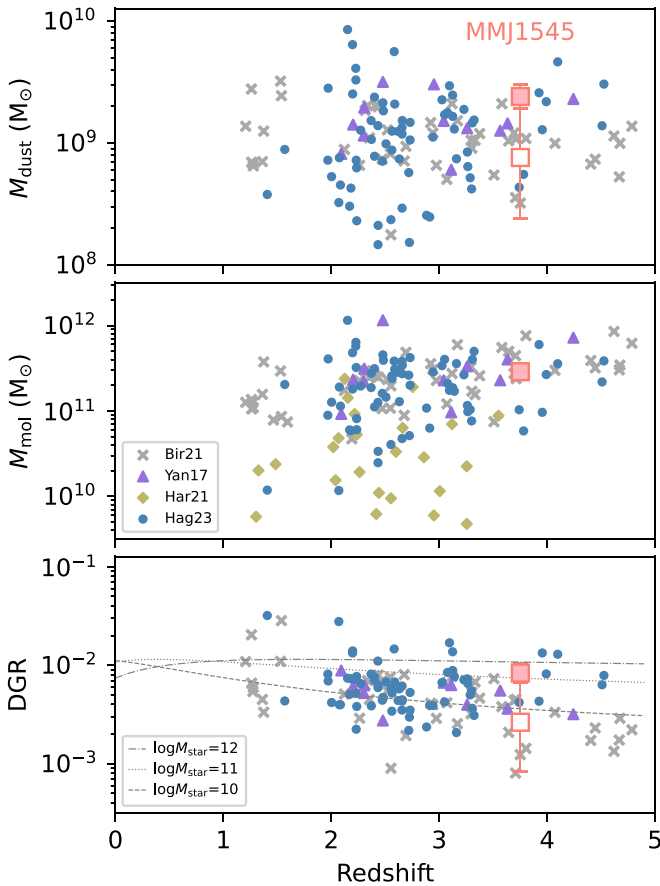
Figure 5. The dust mass, molecular gas mass, and dust-to-gas mass ratio (DGR) of MM J1545 (red filled square) in comparison with lensed (J. E. Birkin et al. 2021, denoted as Bir21) and unlensed (C. Yang et al. 2017; K. C. Harrington et al. 2021; M. Hagimoto et al. 2023, denoted as Yan17, Har21, and Hag23, respectively) submillimeter-bright galaxies as a function of redshift. The masses are corrected for lensing. We assume $\alpha_{CO} = 4.0 M_\odot$ (K km s^{-1} pc^2)$^{-1}$ and the same CO excitation ladder as K. C. Harrington et al. (2021) for a fair comparison. The red open square indicates the dust mass and DGR of MM J1545 with an assumption of a possible lower dust emissivity ($\kappa_\star = 0.11$ cm^2 g^{-1}; see Section 4.2). The dashed, dotted, and dashed–dotted curves represent predicted redshift evolution of DGRs with stellar masses of $\log M_{star}/M_\odot = 10$, 11, and 12, respectively (R. Genzel et al. 2015; L. J. Tacconi et al. 2018).

$\kappa_\star(\nu/\nu_\star)^{\beta_{dust}}$, with $(\kappa_\star, \nu_\star)$ as (10.41 cm^2 g^{-1}, 1900 GHz) from B. T. Draine (2003), the lensed and delensed dust masses are inferred to be $\log M_{dust}/M_\odot = 10.2 \pm 0.1$ and 9.4 ± 0.1, respectively. As shown in the top panel of Figure 5, the intrinsic dust mass of MM J1545 is large even compared with those of the largest dust reservoirs at $z \sim 4$, such as lensed SMGs from the SPT (C. Yang et al. 2017) and Herschel surveys (M. Hagimoto et al. 2023), as well as unlensed SMGs (J. E. Birkin et al. 2021) from AS2COSMOS (J. M. Simpson et al. 2020), AS2UDS (S. M. Stach et al. 2019), and ALESS (J. A. Hodge et al. 2013). This could, however, have a systematic uncertainty depending on choice of the dust mass absorption coefficient. The $\kappa_\star$ value often employed at 850 μm (i.e., $\nu_\star = 353$ GHz) ranges from 0.04 cm^2 g^{-1} (B. T. Draine & H. M. Lee 1984) to 0.3 cm^2 g^{-1} (J. S. Mathis & G. Whiffen 1989), with an intermediate value of 0.11 cm^2 g^{-1} (R. H. Hildebrand 1983), which gives $\kappa_\star \approx 1$–8 cm^2 g^{-1} with an intermediate value of ≈ 3 cm^2 g^{-1} at $\nu_\star = 1900$ GHz if assuming $\beta_{dust} = 1.95$. In this case, the dust mass may be reduced by ~ 0.5 dex, yielding an

intrinsic dust mass of $\log M_{dust}/M_\odot = 8.9 \pm 0.5$, where the error includes the systematic uncertainty arising from the choice of $\kappa_\star$.

In addition, the intrinsic molecular mass is estimated to be large. The apparent molecular masses estimated from CO (2–1) and (4–3) are $M_{mol} \approx 1.9 \times 10^{12} M_\odot$ and $1.5 \times 10^{12} M_\odot$ if we assume CO (2–1)-to-CO (1–0) and CO (4–3)-to-CO (1–0) brightness temperature ratios found in Planck-selected SMGs ($R_{21} = 0.88 \pm 0.07$ and $R_{41} = 0.52 \pm 0.14$, respectively; K. C. Harrington et al. 2021) and a CO (1–0)-to-M_{mol} conversion factor $\alpha_{CO} = 4.0$ $M_\odot$ (K km s^{-1} pc^2)$^{-1}$ (L. Dunne et al. 2022; see Table 1). This indicates an intrinsic molecular mass of $\log M_{mol}/M_\odot \approx 11.5$, although it could decrease by ~ 0.5 dex depending on the choice of α_{CO}. This is comparable to the molecular masses found in the SMG population at $z \sim 4$, as shown in the middle panel of Figure 5.

Along with the intrinsic SFR, the molecular gas depletion timescale is estimated to be ~ 0.4 Gyr. This appears to be greater than those found in the SPT sources at $z \sim 4$ (C. Reuter et al. 2020) whereas it is more similar to those in coeval ($z \sim 4$) main-sequence galaxies (A. Saintonge et al. 2013). This trend is consistent with that found in the Schmidt–Kennicutt relation of dusty star-forming galaxies (M. Hagimoto et al. 2023), where 71 Herschel-selected bright SMGs were compared with the SPT and main-sequence galaxies. This implies that star formation in MM J1545 is not very bursty, which is consistent with the fact that the dust temperature is relatively low.

The intrinsic dust and molecular masses ($\log M_{dust}/M_\odot \approx 9.4$ and $\log M_{mol}/M_\odot \approx 11.5$) give the inferred dust-to-gas mass ratio (DGR) of DGR ≈ 0.0083. This value is even higher than that of the Milky Way and is among the highest end of the DGR distribution found in bright SPT and Herschel sources (C. Yang et al. 2017; M. Hagimoto et al. 2023; see also C. Péroux & J. C. Howk 2020), as shown in the bottom panel of Figure 5. The inferred sum of gas and solid-phase metallicity would be at least $12 + \log(O/H) \gtrsim 8.5$ or $Z \gtrsim 0.6 Z_\odot$ following the relation of C. Péroux & J. C. Howk (2020) and is likely to be $12 + \log(O/H) \gtrsim 8.9$ or $Z \gtrsim 1 Z_\odot$ if the dust-to-metal mass ratio is as high as $\lesssim 0.4$ (C. Péroux & J. C. Howk 2020). The high DGR or metallicity at $z \sim 4$ is indicative of the presence of an underlying massive stellar component of MM J1545, which is not seen in the current optical and NIR images. The curves in the bottom panel of Figure 5 show the DGRs expected for the stellar components with a stellar mass of $\log M_{star}/M_\odot = 10$, 11, and 12. This suggests that MM J1545 should have a stellar component with at least $\gtrsim 10^{10} M_\odot$ and perhaps $\sim 10^{11} M_\odot$. We note that the DGR may be smaller by ~ 0.5 dex if the smaller value is allowed for dust mass as we saw before. If we take $\log M_{dust}/M_\odot \approx 8.9$, then the DGR is estimated to be DGR ≈ 0.0027, which is comparable to the typical values found in lensed and unlensed SMGs or DSFGs at $z \sim 4$ but still indicates the highly enriched interstellar medium (ISM) compared to coeval galaxies in general.

5. Conclusions

We report detections of two emission lines at 48.5 and 97.0 GHz in an $S_{1.1\,mm} = 44$ mJy SMG, MM J154506.4 −344318 (MM J1545), using ATCA and the Nobeyama 45 m telescope. We also find the blueshifted part of an emission line at ≈ 218.3 GHz using archival ALMA data. Together with the photometric redshift estimates and the ratio between the line and IR luminosities, we conclude that they are most likely to be the (2–1), (4–3), and (9–8) rotational transitions of ^{12}CO at

redshift $z = 3.753 \pm 0.001$. The ALMA continuum imaging confirms MM J1545 to be a gravitationally lensed SMG with a magnification factor of $\mu_g \approx 7$, suggesting the presence of an intrinsically massive, chemically enriched reservoir of cool ISM at $z = 3.75$, or 1.6 Gyr after the Big Bang.

If assuming a nominal magnification of $\mu_g = 6.6$ for MM J1545, the intrinsic dust and molecular masses are still high even after correcting for magnification ($\log M_{\rm dust}/M_\odot \approx 9.4$ and $\log M_{\rm mol}/M_\odot \approx 11.5$), which is indicative of a high DGR (≈ 0.0083). Such a starburst galaxy with a chemically enriched reservoir of cool ISM at $z \sim 4$ is rare even compared with existing samples and will provide a unique opportunity to investigate spatially resolved properties of ISM and star formation in the early Universe. This work, however, only adds one additional source to existing samples and thus does not provide stringent constraints on the general properties of the extremely bright population of dusty star-forming galaxies owing to a small sample size. Expanding the extremely bright samples at $z \gtrsim 4$ will address the earlier chemical enrichment more thoroughly. Future (sub) millimeter facilities for wide-field imaging (e.g., TolTEC; G. W. Wilson et al. 2020) and wideband spectroscopy (e.g., DESHIMA 2.0, FINER; M. Rybak et al. 2022; A. Taniguchi et al. 2022; Y. Tamura et al. 2024) will allow us to investigate this further. In addition, stellar and nebular properties in the rest-frame optical are also necessary for comprehensive understanding. Higher-resolution ALMA and James Webb Space Telescope imaging will play an important role in fully characterizing the physical properties of MM J1545.

ORCID iDs

Yoichi Tamura ⓘ https://orcid.org/0000-0003-4807-8117
Akio Taniguchi ⓘ https://orcid.org/0000-0002-9695-6183
Tom J. L. C. Bakx ⓘ https://orcid.org/0000-0002-5268-2221
Itziar De Gregorio-Monsalvo ⓘ https://orcid.org/0000-0003-4518-407X
Masato Hagimoto ⓘ https://orcid.org/0000-0001-8083-5814
Ryohei Kawabe ⓘ https://orcid.org/0000-0002-8049-7525
Kotaro Kohno ⓘ https://orcid.org/0000-0002-4052-2394
Kouichiro Nakanishi ⓘ https://orcid.org/0000-0002-6939-0372
Tatsuya Takekoshi ⓘ https://orcid.org/0000-0002-4124-797X
Yoshito Shimajiri ⓘ https://orcid.org/0000-0001-9368-3143
Takashi Tsukagoshi ⓘ https://orcid.org/0000-0002-6034-2892
Bunyo Hatsukade ⓘ https://orcid.org/0000-0001-6469-8725
Daisuke Iono ⓘ https://orcid.org/0000-0002-2364-0823
Kazuya Saigo ⓘ https://orcid.org/0000-0003-1549-6435
Masao Saito ⓘ https://orcid.org/0000-0003-0769-8627

References

Astropy Collaboration, Price-Whelan, A. M., Lim, P. L., et al. 2022, ApJ, 935, 167
Astropy Collaboration, Price-Whelan, A. M., Sipőcz, B. M., et al. 2018, AJ, 15, 123
Astropy Collaboration, Robitaille, T. P., Tollerud, E. J., et al. 2013, A&A, 558, A33
Baars, J. W. M. 2007, The Paraboloidal Reflector Antenna in Radio Astronomy and Communication (Berlin: Springer),
Birkin, J. E., Weiss, A., Wardlow, J. L., et al. 2021, MNRAS, 501, 3926
Blain, A. W., Smail, I., Ivison, R. J., Kneib, J. P., & Frayer, D. T. 2002, PhR, 369, 111
Bothwell, M. S., Smail, I., Chapman, S. C., et al. 2013, MNRAS, 429, 3047
CASA Team, Bean, B., Bhatnagar, S., et al. 2022, PASP, 134, 114501
Casey, C. M., Narayanan, D., & Cooray, A. 2014, PhR, 541, 45
da Cunha, E., Groves, B., Walter, F., et al. 2013, ApJ, 766, 13
Draine, B. T. 2003, ApJ, 598, 1017
Draine, B. T., & Lee, H. M. 1984, ApJ, 285, 89
Dunne, L., Maddox, S. J., Papadopoulos, P. P., Ivison, R. J., & Gomez, H. L. 2022, MNRAS, 517, 962
Eales, S., Dunne, L., Clements, D., et al. 2010, PASP, 122, 499
Ezawa, H., Kawabe, R., Kohno, K., & Yamamoto, S. 2004, Proc. SPIE, 5489, 763
Ezawa, H., Kohno, K., Kawabe, R., et al. 2008, Proc. SPIE, 7012, 701208
Fujimoto, S., Kohno, K., Ouchi, M., et al. 2024, ApJS, 275, 36
Garratt, T. K., Geach, J. E., Tamura, Y., et al. 2023, MNRAS, 520, 3669
Geach, J. E., Dunlop, J. S., Halpern, M., et al. 2017, MNRAS, 465, 1789
Genzel, R., Tacconi, L. J., Lutz, D., et al. 2015, ApJ, 800, 20
Gururajan, G., Béthermin, M., Theulé, P., et al. 2022, A&A, 663, A22
Hagimoto, M., Bakx, T. J. L. C., Serjeant, S., et al. 2023, MNRAS, 521, 5508
Harrington, K. C., Weiss, A., Yun, M. S., et al. 2021, ApJ, 908, 95
Harris, A. I., Baker, A. J., Frayer, D. T., et al. 2012, ApJ, 752, 152
Harris, C., Millman, K. J., van der Walt, S. J., et al. 2020, Natur, 585, 357
Hatsukade, B., Kohno, K., Yamaguchi, Y., et al. 2018, PASJ, 70, 105
Hildebrand, R. H. 1983, QJRAS, 24, 267
Hodge, J. A., Karim, A., Smail, I., et al. 2013, ApJ, 768, 91
Hoyer, S., & Hamman, J. 2017, JORS, 5, 10
Hunter, J. D. 2007, CSE, 9, 90
Ikarashi, S., Kohno, K., Aguirre, J. E., et al. 2011, MNRAS, 415, 3081
Ikeda, M., Nishiyama, K., Ohishi, M., & Tatematsu, K. 2001, in ASP Conf. Ser. 238, Astronomical Data Analysis Software and Systems X, ed. F. R. Harnden, F. A. Primini, & H. E. Payne (San Francisco, CA: ASP), 522
Iono, D., Hatsukade, B., Kohno, K., et al. 2012, PASJ, 64, L2
Iono, D., Wilson, C. D., Yun, M. S., et al. 2009, ApJ, 695, 1537
Kennicutt, R. C., & Evans, N. J. 2012, ARA&A, 50, 531
Kohno, K., Tamura, K., & Hatsukade, B. 2008, in ASP Conf. Ser. 399, Panoramic Views of Galaxy Formation and Evolution, ed. T. Kodama, T. Yamada, & K. Aoki (San Francisco, CA: ASP), 264
Kroupa, P., Tout, C. A., & Gilmore, G. 1993, MNRAS, 262, 545

La Barbera, F., de Carvalho, R. R., de La Rosa, I. G., & Lopes, P. A. A. 2010, MNRAS, 408, 1335

Larson, R. B. 1969, MNRAS, 145, 271

Litke, K. C., Marrone, D. P., Spilker, J. S., et al. 2019, ApJ, 870, 80

Mathis, J. S., & Whiffen, G. 1989, ApJ, 341, 808

McKinney, W. 2010, in Proc. 9th Python in Science Conf., ed. S. van der Walt & J. Millman (Austin, TX: SciPy), 56

Michałowski, M., Hjorth, J., & Watson, D. 2010, A&A, 514, A67

Nakajima, T., Kimura, K., Nishimura, A., et al. 2013, PASP, 125, 252

Negrello, M., Hopwood, R., De Zotti, G., et al. 2010, Sci, 330, 800

Newville, M., Otten, R., Nelson, A., et al. 2023, lmfit/lmfit-py: v1.2.2, Zenodo, doi:10.5281/zenodo.8145703

Oguri, M. 2010, PASJ, 62, 1017

Omont, A., Neri, R., Cox, P., et al. 2011, A&A, 530, L3

Péroux, C., & Howk, J. C. 2020, ARA&A, 58, 363

Reuter, C., Vieira, J. D., Spilker, J. S., et al. 2020, ApJ, 902, 78

Rybak, M., Bakx, T., Baselmans, J., et al. 2022, JLTP, 209, 766

Rybak, M., Hodge, J. A., Vegetti, S., et al. 2020, MNRAS, 494, 5542

Saintonge, A., Lutz, D., Genzel, R., et al. 2013, ApJ, 778, 2

Saito, M., de Gregorio, I., & Team, S.O.L.A. 2015, in ASP Conf. Ser. 499, Revolution in Astronomy with ALMA: The Third Year, ed. D. Iono et al. (San Francisco, CA: ASP), 215

Santamarìa-Miranda, A., de Gregorio-Monsalvo, I., Plunkett, A. L., et al. 2021, A&A, 646, A10

Sault, R. J., Teuben, P. J., & Wright, M. C. H. 1995, in ASP Conf. Ser. 77 Astronomical Data Analysis Software and Systems IV, ed. R. A. Shaw, H. E. Payne, & J. J. E. Hayes (San Francisco, CA: ASP), 433

Scott, K. S., Wilson, G. W., Aretxaga, I., et al. 2012, MNRAS, 423, 575

Silva, L., Granato, G. L., Bressan, A., & Danese, L. 1998, ApJ, 509, 103

Simpson, J. M., Smail, I., Dudzevičiuūė, U., et al. 2020, MNRAS, 495, 3409

Spilker, J. S., Aravena, M., Marrone, D. P., et al. 2015, ApJ, 811, 124

Spilker, J. S., Marrone, D. P., Aguirre, J. E., et al. 2014, ApJ, 785, 149

Stach, S. M., Dudzevičiūtė, U., Stach, I., et al. 2019, MNRAS, 487, 4648

Swinbank, A. M., Smail, I., Longmore, S., et al. 2010, Natur, 464, 733

Tacconi, L. J., Genzel, R., Saintonge, A., et al. 2018, ApJ, 853, 179

Takekoshi, T., Tamura, Y., Minamidani, T., et al. 2013, ApJL, 774, L30

Tamura, Y., Kawabe, R., Shimajiri, Y., et al. 2015, ApJ, 808, 121

Tamura, Y., Saito, T., Tsuru, T. G., et al. 2014, ApJL, 781, L39

Tamura, Y., Sakai, T., Kawabe, R., et al. 2024, Proc. SPIE, 13102, 131020G

Taniguchi, A., Bakx, T. J. L. C., Baselmans, J. J. A., et al. 2022, JLTP, 209, 278

The pandas development team 2023, pandas-dev/pandas: Pandas, v1.5.3, Zenodo, doi:10.5281/zenodo.7549438

Tomida, K., Machida, M. N., Saigo, K., Tomisaka, K., & Matsumoto, T. 2010, ApJL, 725, L239

Tomida, K., Tomisaka, K., Matsumoto, T., et al. 2013, ApJ, 763, 6

Tully, R. B., & Fisher, J. R. 1977, A&A, 54, 661

Vieira, J. D., Crawford, T. M., Switzer, E. R., et al. 2010, ApJ, 719, 763

Vieira, J. D., Marrone, D. P., Chapman, S. C., et al. 2013, Natur, 495, 344

Weiß, A., Kovács, A., Coppin, K., et al. 2009, ApJ, 707, 1201

Wilson, G. W., Abi-Saad, S., Ade, P., et al. 2020, Proc. SPIE, 11453, 1145302

Wilson, G. W., Austermann, J. E., Perera, T. A., et al. 2008, MNRAS, 386, 807

Yang, C., Omont, A., Beelen, A., et al. 2017, A&A, 608, A144

Zhang, Z.-Y., Romano, D., Ivison, R. J., Papadopoulos, P. P., & Matteucci, F. 2018, Natur, 558, 260